JACS JOURNAL OF THE AMERICAN CHEMICAL SOCIETY

Article

Cite This: J. Am. Chem. Soc. 2018, 140, 6921−6930

pubs.acs.org/JACS

Near-Ideal Xylene Selectivity in Adaptive Molecular Pillar[*n*]arene Crystals

Kecheng Jie,[†,⊥] Ming Liu,[‡,⊥] Yujuan Zhou,[†] Marc A. Little,[‡] Angeles Pulido,[§] Samantha Y. Chong,[‡] Andrew Stephenson,[‡] Ashlea R. Hughes,[∥] Fumiyasu Sakakibara,[¶] Tomoki Ogoshi,[¶,⊗,#] Frédéric Blanc,[∥] Graeme M. Day,[*,§] Feihe Huang,[*,†] and Andrew I. Cooper[*,‡]

[†]State Key Laboratory of Chemical Engineering, Center for Chemistry of High-Performance & Novel Materials, Department of Chemistry, Zhejiang University, Hangzhou 310027, People's Republic of China

[‡]Materials Innovation Factory and Department of Chemistry, University of Liverpool, 51 Oxford Street, Liverpool L7 3NY, United Kingdom

[§]Computational Systems Chemistry, School of Chemistry, University of Southampton, Southampton SO17 1BJ, United Kingdom

[∥]Department of Chemistry and Stephenson Institute for Renewable Energy, University of Liverpool, Crown Street, Liverpool L69 7ZD, United Kingdom

[¶]Graduate School of Natural Science and Technology, Kanazawa University, Kakuma-machi, Kanazawa, Ishikawa 920-1192, Japan

[⊗]WPI Nano Life Science Institute, Kanazawa University, Kakuma-machi, Kanazawa, Ishikawa 920-1192, Japan

[#]JST, PRESTO, 4-1-8 Honcho, Kawaguchi, Saitama 332-0012, Japan

Supporting Information

ABSTRACT: The energy-efficient separation of alkylaromatic compounds is a major industrial sustainability challenge. The use of selectively porous extended frameworks, such as zeolites or metal−organic frameworks, is one solution to this problem. Here, we studied a flexible molecular material, perethylated pillar[*n*]arene crystals (n = 5, 6), which can be used to separate C8 alkylaromatic compounds. Pillar[6]arene is shown to separate *para*-xylene from its structural isomers, *meta*-xylene and *ortho*-xylene, with 90% specificity in the solid state. Selectivity is an intrinsic property of the pillar[6]arene host, with the flexible pillar[6]arene cavities adapting during adsorption thus enabling preferential adsorption of *para*-xylene in the solid state. The flexibility of pillar[6]arene as a solid sorbent is rationalized using molecular conformer searches and crystal structure prediction (CSP) combined with comprehensive characterization by X-ray diffraction and ^{13}C solid-state NMR spectroscopy. The CSP study, which takes into account the structural variability of pillar[6]arene, breaks new ground in its own right and showcases the feasibility of applying CSP methods to understand and ultimately to predict the behavior of soft, adaptive molecular crystals.

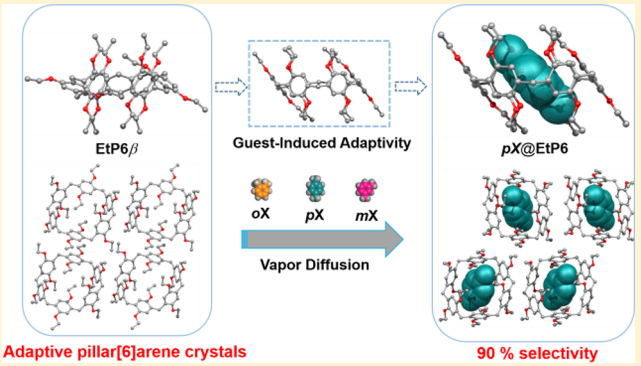

1. INTRODUCTION

With the expanding global demand for petrochemical feedstocks, the development of new materials that reduce the environmental impact of chemical processing is important. Improving the efficiency of the separation and refining of aromatic hydrocarbons is of particular importance, given the large volumes of these compounds that are used as starting materials in the chemical industry.[1] One of the most challenging separations is that of xylene isomers (*ortho*, *meta* and *para*, hereafter referred to as ***o*X**, ***m*X** and ***p*X**), which was classified by Sholl as one of the "seven chemical separations to change the world".[2] These xylene isomers are obtained from crude oil by catalytic reforming, by toluene disproportionation, and by the distillation of pyrolysis gasoline.[3] They act as antiknocking additives in gasoline and they also are important chemical feedstocks for phthalic anhydrides and phthalonitriles. ***p*X** is the most important isomer: it is primarily used as a feedstock with purity requirement of >99%, for terephthalic acid and dimethyl terephthalate production; these compounds are then used to prepare polyester fibers and polyethylene terephthalate (PET) resins for beverage bottles.[4−8] The energy-efficient separation of ***p*X** from ***o*X** and ***m*X** with high purity is therefore important in large-scale plastics production.

***p*X**, ***o*X** and ***m*X** have similar boiling points (Table S1, Supporting Information), but the difference in their freezing points allows separation by fractional crystallization. ***p*X** has the highest melting point because ***p*X** molecules can stack more

Received: March 7, 2018
Published: May 12, 2018

DOI: 10.1021/jacs.8b02621
J. Am. Chem. Soc. 2018, 140, 6921−6930

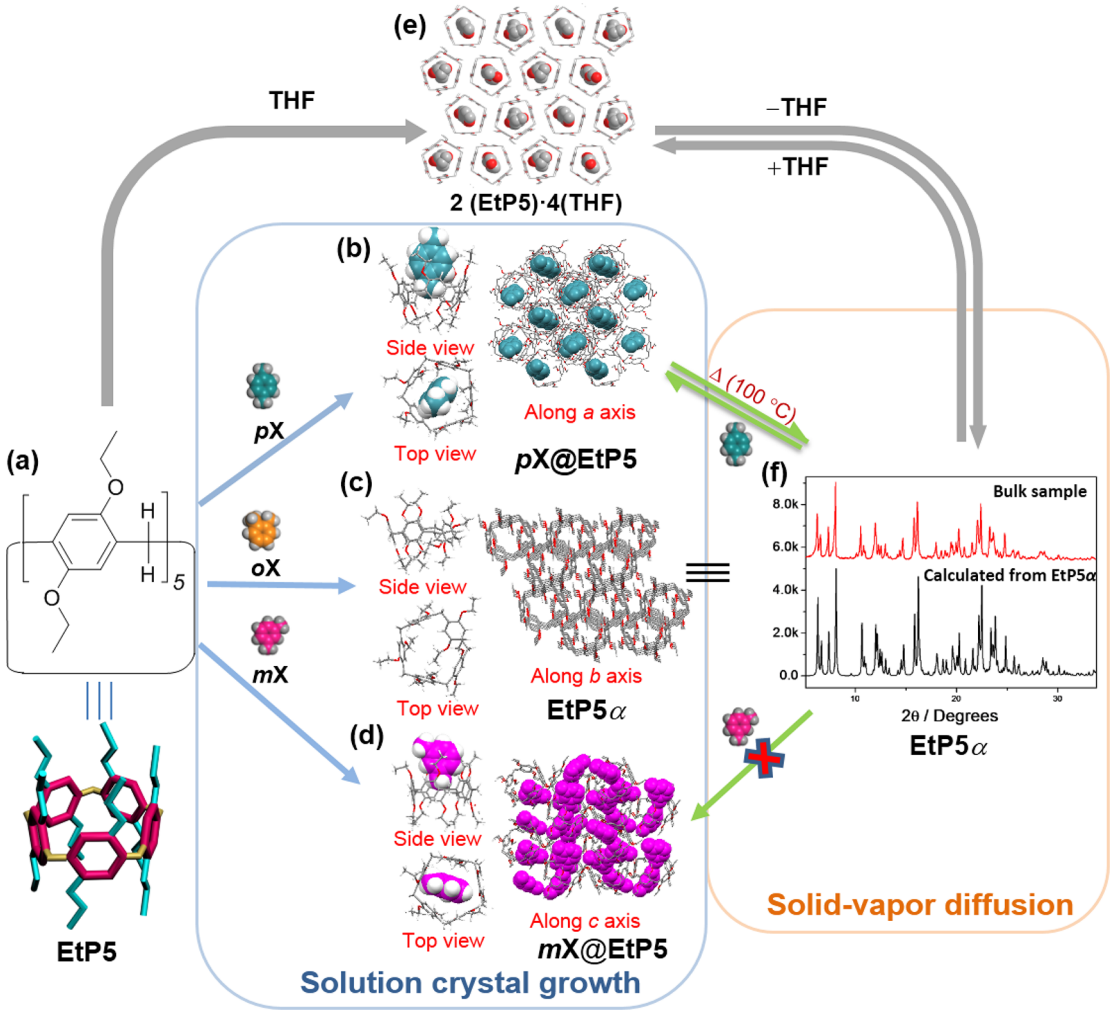

Figure 1. Scheme summarizing the interconversion of the various pillar[5]arene−xylene host−guest crystal structures in solution and the solid state. (a) Chemical structure of perethylated pillar[5]arene (**EtP5**). Single crystal structure: (b) ***p*X@EtP5**, (c) guest free **EtP5*α***, obtained after crystallization of **EtP5** from an ***o*X** solution, (d) ***m*X@EtP5** and (e) 2(**EtP5**)·4(**THF**). (f) On activation, the **EtP5** solvate structures (THF, ***p*X** or ***m*X**) transfrom to the guest free, thermally stable phase, **EtP5*α***, as confirmed by powder X-ray diffraction pattern. Bottom: PXRD patterns of **EtP5*α*** simulated from desolvated single crystal structure of **EtP5*α***, obtained by slow evaporation of ***o*X** from an ***o*X-EtP5** solution; Top: recrystallized from THF and desolvated at 60 °C under dynamic vacuum.

efficiently; pure ***p*X** crystals are hence the first to crystallize from the solution. However, the energy requirement for fractional crystallization is high because of the need to cool large quantities of material to about −53 °C.[9] Selective adsorption of xylene isomers in the pores of ordered crystalline microporous materials is an energy-efficient alternative to fractional crystallization.[10−16] However, identifying a suitable porous material for xylene separation is challenging due to similar molecular sizes of the three isomers. Moreover, most potential candidate crystalline porous frameworks are built using reversible chemistry and they are not stable enough for industrial application: the loss of porosity is typically irreversible and catastrophic for this separation.

Pillar[*n*]arenes (*n* = 5−15) have emerged as a novel class of supramolecular hosts since they were first reported in 2008.[17−40] Their host−guest properties have been investigated using a diverse range of guest molecules, including hydrocarbons.[32−34,40] For example, we reported the host−guest chemistry between alkyl chains and pillar[5]arenes due to CH/π interactions.[32,33] Yang et al. reported a biphenyl-extended pillar[*n*]arene for an efficient selective inclusion of toluene and ***m*X**.[34] With these unique features, we and other groups found that pillararene crystals can be used for gas storage and hydrocarbon separations.[37−40] For example, we recently reported that a perethylated pillar[6]arene can act as a separation material to purify styrene from a mixture of styrene and ethylbenzene.[39] That separation was based on a solid-state recrystallization process, rather than an adsorptive separation that uses a material with permanent, pre-existing pores. Styrene molecules were selectively adsorbed in extrinsic voids in the crystal structure: that is, the host−guest properties of the pillar[*n*]arene cavity were not directly exploited.

We show here that the intrinsic cavity of pillar[*n*]arenes can be utilized in molecular separations of important C8 hydrocarbon feedstocks. The shape selectivity of two perethylated pillar[*n*]arenes with different cavity sizes were investigated (where *n* = 5 or 6, referred to hereafter as **EtP5** and **EtP6**). We found that **EtP6** adsorbs ***p*X** selectively from a mixture of xylene isomers, both in solution and in the solid state. Selective adsorption of ***p*X** is an intrinsic feature of the **EtP6** host with the flexible **EtP6** cavities adapting during adsorption, thus enabling preferential adsorption of ***p*X** in the crystalline state,

DOI: 10.1021/jacs.8b02621
J. Am. Chem. Soc. 2018, 140, 6921−6930

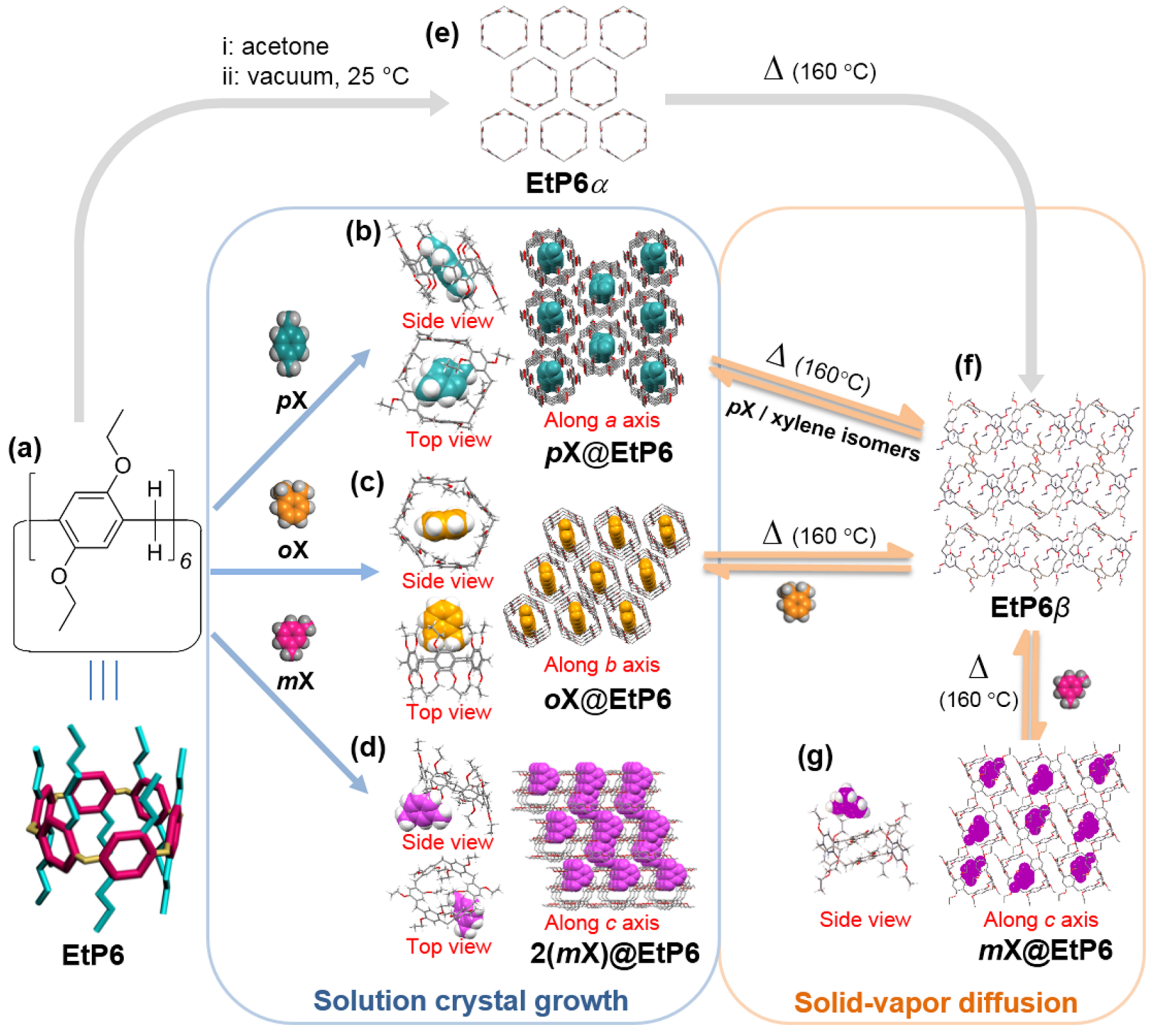

Figure 2. Scheme summarizing the interconversion of the various pillar[6]arene–xylene host–guest crystal structures in solution and the solid state. (a) Chemical structure of perethylated pillar[6]arene (**EtP6**). Single crystal structures: (b) ***p*X@EtP6**, (c) 2(***m*X**)@**EtP6** and (d) ***o*X@EtP6**. (e) The metastable, **EtP6***α*, which has a 1D pore structure, is obtained by carefully activating the acetone solvate.[32] (f) By thermally desolvating **EtP6** structures at 160 °C (acetone, ***p*X**, ***o*X** or ***m*X**), a stable phase, referred to as **EtP6***β*, is obtained. (g) When **EtP6***β* is exposed to ***m*X** vapor, a new structure, ***m*X@EtP6**, is found.

unlike our previous styrene study.[39] The flexibility of **EtP6** can be rationalized computationally by exploring the conformational energy landscape, and this explains the flexibility that we observe by crystallography and solid-state NMR. The observed combination of adsorptive separation and guest-induced restructuring is similar to flexible MOFs[10,41] but reported here for an adaptive molecular crystal. We exploited this selectivity to develop an adsorption/desorption process where ***p*X** could be separated from a 1:1:1 mixture of the three xylene isomers with a purity of 99.1%.

2. RESULTS AND DISCUSSION

Structural Analysis of EtP5 with Xylene Isomers in Solution and the Solid State. First, the host–guest chemistry of **EtP5** with ***p*X**, ***m*X** or ***o*X** was investigated. These three xylene isomers have different dimensions, and the size of these approach the size of the **EtP5** cavity (Figure S1). In the 1:1 host–guest crystal structure of ***p*X@EtP5**, the ***p*X** guest is only partially accommodated in the **EtP5** cavity with the aromatic pillars of **EtP5** adopting a bowl shape to accommodate the ***p*X** guest (Figure 1b). In the crystal structure of ***m*X@EtP5**, we found ordered ***m*X** guest molecules with one of the methyl groups pointing toward the center of the **EtP5** cavity, whereas the second, *meta* substituted, methyl group does not fit in the **EtP5** cavity (Figure 1d). When **EtP5** was crystallized from ***o*X**, no ***o*X** was found in the structure. Instead, the structure is guest free and referred hereafter as, **EtP5***α* (Figure 1c). During this study, we activated **EtP5** material by desolvating a THF solvate. The experimental powder X-ray diffraction (PXRD) pattern of activated **EtP5** material matches the simulated PXRD pattern of **EtP5***α* (Figure 1f). Hence, **EtP5***α* is the structure of the activated material.

Structural Analysis of EtP6 with Xylene Isomers in Solution and the Solid State. After determining the solid-state host–guest chemistry of **EtP5** and the xylene isomers, we next investigated **EtP6**. The cavity size of **EtP6** is larger; hence, it is more likely that the three xylene isomers can fit within the **EtP6** cavity. Single crystal structures of **EtP6** with ***o*X**, ***m*X** and ***p*X** were all obtained. In the 1:1 host–guest crystal structure of ***p*X@EtP6**, one ***p*X** molecule is located almost perfectly in the center of the **EtP6** cavity (Figure 2b). This host–guest complex is stabilized by offset π–π stacking interactions between ***p*X** and two aromatic rings of **EtP6** (Figure 2b). The hexagonal pillar

DOI: 10.1021/jacs.8b02621
J. Am. Chem. Soc. 2018, 140, 6921–6930

structure of **EtP6** contributes to the formation of infinite 1D channels running through the aligned macrocycles that are filled with ordered ***p*X** guests (Figure 2b). The 2:1 solvated crystal structure of **EtP6** with ***m*X**, 2(***m*X**)@**EtP6**, is markedly different. Two opposite aromatic pillars of **EtP6** are turned perpendicular with respect to their neighboring pillars (Figure 2d). Hence, in 2(***m*X**)@**EtP6**, **EtP6** has a deformed cavity that is too small to fully accommodate a ***m*X** guest (Figure 2d). When crystallized from ***o*X**, **EtP6** formed a 1:1 host–guest complex, ***o*X**@**EtP6** (Figure 2c), where the **o**X molecules are disordered within the **EtP6** cavity with the *ortho*-substituted methyl groups located in the center of the cavity. The hexagonal structure of **EtP6** forms infinite intrinsic 1D channels that are filled with ***o*X** guests, broadly comparable with ***p*X**@**EtP6**, but again, the **EtP6** adopts a different conformation. In ***p*X**@**EtP6**, the **EtP6** pillars are angled to maximize $\pi-\pi$ stacking interactions with the ***p*X** guest. By contrast, in ***o*X**@**EtP6** the pillars are all aligned and the ***o*X** guest is disordered.

Because of the apparently favorable host–guest interactions (Figure 2b), we speculated that **EtP6** might crystallize preferentially with ***p*X** in the presence of ***o*X** and ***m*X**. Indeed, when **EtP6** was crystallized from a 1:1:1 (v:v:v) mixture of the three xylene isomers, we only obtained single crystals of ***p*X**@**EtP6**, showing that **EtP6** selectively captures ***p*X** in its cavity from solution.

These single crystal structure studies suggested that **EtP6**, with its hexagonal shape and larger cavity than **EtP5**, might be more efficient for the dynamic separation of ***p*X** from ***o*X** and ***m*X**. To test this, samples of **EtP5** and **EtP6** were activated and crystallized from tetrahydrofuran and acetone, respectively. We also followed the activation of **EtP6** by both single crystal X-ray diffraction (SC-XRD) and PXRD. For **EtP6**, careful removal of acetone from the **EtP6** solvate at room temperature afforded **EtP6***α*, which has been characterized before by PXRD.[39] Here, we found that thermal activation of the **EtP6** solvate at temperatures of ≥140 °C resulted in the formation of a new phase, **EtP6***β* (Figure 2f, S7–S10). The single crystal structure of **EtP6***β* contains a new **EtP6** conformer where the aromatic pillars are no longer aligned, and this rearrangement results in a loss of the **EtP6** cavity (Figure S10).

A similar phase transition process was also observed during the desolvation of ***p*X**@**EtP6**. As shown in Figure 3a, peaks related to a new phase started to appear upon heating to around 140 °C in the *in situ* desolvation PXRD experiment, and the phase transformation was completed at 160 °C. After cooling this sample to 20 °C, the structure of the bulk materials was determined to be **EtP6***β*, which was found to be stable at ambient temperature. This process was studied by thermogravimetric analysis (TGA) and differential scanning calorimetry (DSC), as shown in Figure 3b. In the DSC curve of ***p*X**@**EtP6**, a broad peak between 146 and 157 °C represents the loss of one ***p*X** molecule from the host–guest complex, in line with the weight loss observed by TGA, followed by a phase transformation. Comparison of the TGA and DSC traces (Figure 3b) suggests that this phase transition occurs when essentially all of the ***p*X** guests have been removed.

The ^{13}C cross-polarization (CP) magic angle spinning (MAS) NMR spectra of the three guest free pillararenes (**EtP5***α*, **EtP6***α* and **EtP6***β*) are shown in Figure 4 and provide structural information regarding the asymmetric unit. **EtP6***β* shows a range of narrow and well resolved resonances that could be assembled into the six different chemical subgroups for **EtP6**, corresponding to the chemically distinct carbons

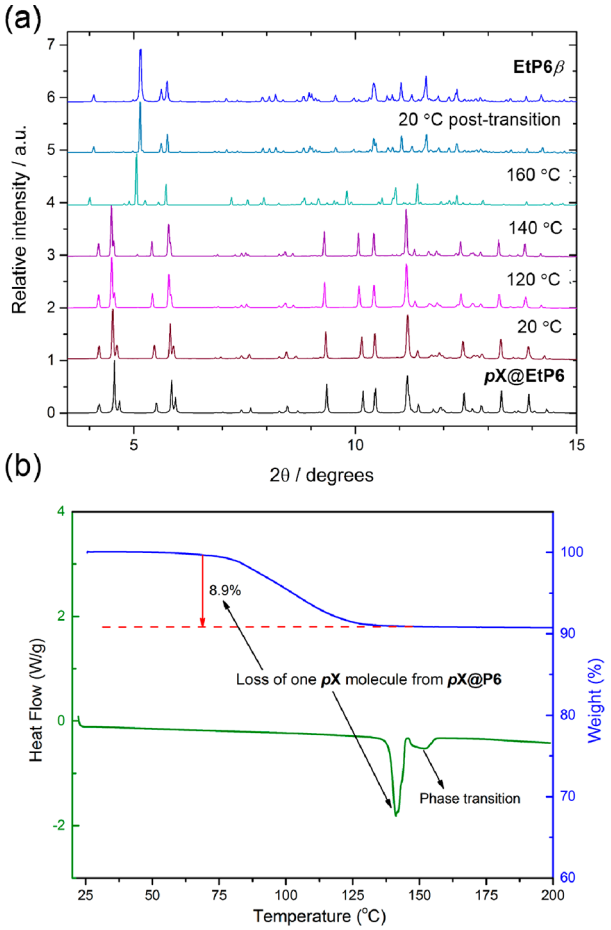

Figure 3. (a) *In situ* variable temperature PXRD patterns for ***p*X**@**EtP6** showing thermal transformation at 160 °C. (b) Thermogravimetric analysis (TGA) (blue) and differential scanning calorimetry (DSC) (green) studies of ***p*X**@**EtP6**. The difference in ***p*X** desolvation temperature between TGA and DSC experiments is a result of the different heating conditions (open pan under N_2 flow for TGA, and sealed pan for DSC).

environments; for example, the quaternary carbon atoms bonded to oxygens in O**C**^{IV} appear in the 149–155 ppm region. The assignment given is based on ^{13}C-editing NMR experiments and known ^{13}C chemical shift values from the literature.[42] With remarkably sharp lines acquired at natural abundance, the carbon connectivities obtained from the two-dimensional ^{13}C–^{13}C through-bond INADEQUATE[43−45] correlation spectrum (Figure S11a) further confirmed the assignment.

The inset in Figure 4c (and the full spectral deconvolution in Figure S14) shows that each environment consists of multiple ^{13}C peaks whose integrations (see Experimental Section) match well with the expected number of nonequivalent carbon atoms in the asymmetric units, as determined by X-ray diffraction (Figure 2f). For example, seven O**C**^{IV} resonances are resolved integrating 1:1:1:1:3:3:2 (from high to low frequency) and matching the expected 12 O**C**^{IV} carbons in **EtP6***β*. Calculations of the ^{13}C chemical shifts of **EtP6***β* was also carried out, and the calculated chemical shifts were compared with the experimental chemical shifts (as shown in Figure S11b). The comparison shows to be in excellent agreement, further validating the spectral assignments. It also provides proof of the good match between the experimentally obtained crystal structures and the

DOI: 10.1021/jacs.8b02621
J. Am. Chem. Soc. 2018, 140, 6921–6930

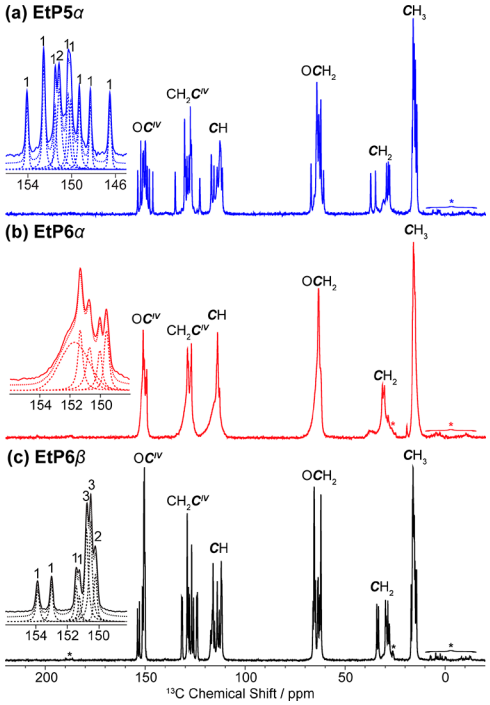

Figure 4. ^{13}C CP MAS NMR spectra of (a) **EtP5***α*, (b) **EtP6***α* and (c) **EtP6***β*. Asterisks (*) denote spinning sidebands. The expansion shows the experimental spectrum (full line), total fit (dotted line) and spectral deconvolution (dashed lines) of the OC^{IV} carbons; all other fits are given in the SI (Figure S12–S14).

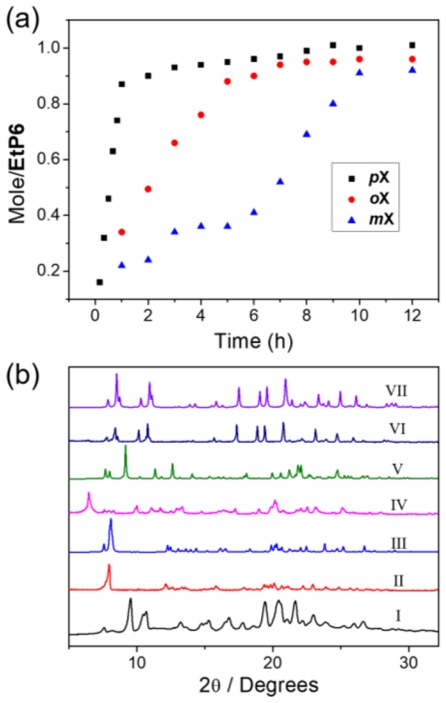

Figure 5. (a) Time-dependent **EtP6***β* solid–vapor sorption plot for single-component xylene isomer vapor. (b) PXRD patterns: (I) **EtP6***β*; (II) **EtP6***β* after uptake of ***o*X** vapor; (III) simulated from single crystal structure of ***o*X@EtP6**; (IV) **EtP6***β* after uptake of ***m*X** vapor; (V) simulated from single crystal structure of 2(***m*X**)**@EtP6**; (VI) **EtP6***β* after uptake of ***p*X** vapor; (VII) simulated from single crystal structure of ***p*X@EtP6**.

calculated conformers (see Crystal Structure Prediction section below).

Similarly, the highly resolved ^{13}C CP MAS NMR spectrum of **EtP5***α* allows each carbon environment to be observed and quantified; there is a good agreement between the deconvoluted spectra and the expected number of non-equivalent carbon atoms in **EtP5***α* (e.g., ten OC^{IV} carbons, Figure 4a and S12). However, by comparison, the resolution of the **EtP6***α* spectrum is much poorer with broader peaks observed (Figure 4b, S13). This indicates that unlike **EtP6***β* and **EtP5***α*, **EtP6***α* is not phase pure, which we attribute to the existence of multiple **EtP6** conformers in the metastable **EtP6***α* activated material and highlights the importance of correlating X-ray diffraction studies with solid-state NMR measurements.

Xylene Vapor-Phase Adsorption Studies. Time-dependent solid–vapor sorption experiments for single-component xylene isomers were carried out for crystalline **EtP5***α* and **EtP6***β*. It was found that **EtP5***α* adsorbed almost the same amount of ***p*X** as **EtP6***β*, but a lower amount of ***m*X** and ***o*X** (Figure S16a). Though **EtP6***β* adsorbed similar amounts of each of the three isomers at equilibrium, the uptake of ***p*X** was much faster than for ***o*X** and ***m*X**, at least in noncompetitive, single-component experiments (Figure 5a). We also carried out PXRD studies to monitor the adsorption of the single xylene isomers by **EtP5***α* (Figure S16b) and **EtP6***β* (Figure 5b). PXRD data indicated that **EtP5***α* transformed into ***p*X@EtP5** after adsorption of ***p*X** (Figure 1f → 1b, and S17). **EtP5***α* showed no structural transformation after exposure to ***o*X** or ***m*X**, suggesting that neither molecule was adsorbed in the bulk by **EtP5***α*. It is possible that crystal surface adsorption accounts for the relatively small uptake of these two isomers (8–10 times lower than ***p*X**; Figure S16a). PXRD data indicate that **EtP6***β*, unlike **EtP5***α*, transforms in the solid state after adsorption of ***o*X**, ***m*X** and ***p*X** (Figure 2 and 5b). After adsorption of ***p*X** and ***o*X**, the PXRD patterns match the simulated PXRD patterns derived from the single crystal structures of ***p*X@EtP6** (Figure 2f → 2b, S18), and ***o*X@EtP6** (Figure 2f → 2c, S19), respectively. The PXRD pattern of **EtP6***β* after adsorption of ***m*X** (Figure 5b, PXRD pattern IV) showed that the structure was neither **EtP6***β* nor 2(***m*X**)**@EtP6** (Figure 5b, PXRD patterns I and V, respectively); rather, **EtP6***β* tranformed to a new phase, that was determined by single crystal X-ray diffraction to be ***m*X@EtP6** (Figure 2f → 2g, S20).

EtP6 can adsorb all three xylene isomers because of its conformational flexibility, which provides a flexible cavity and adaptability in the crystal packing. To determine if **EtP5***α* or **EtP6***β* can discriminate between a mixture of xylene isomers, we carried out time-dependent solid–vapor sorption experiments using a 1:1:1 volumetric ratio of ***o*X**: ***m*X**: ***p*X**. We found that the uptake of xylene isomers by **EtP5***α* was almost negligible under these conditions (Figure S23). The PXRD pattern of activated **EtP5***α* did not transform after exposure to the xylene isomer mixture for 10 h (Figure S25). It can be concluded that the mixture of xylene isomers was not adsorbed in the bulk by **EtP5***α*. Instead, we ascribe the small, substoichiometric uptake of xylene isomers by **EtP5***α* to be surface adsorption on the crystals. It is noteworthy that **EtP5***α* adsorbed neat ***p*X**, whereas ***p*X** was not adsorbed from the xylene isomers mixture. The uptake of xylene by **EtP6***β* was far greater. In fact, **EtP6***β* adsorbed ten times more ***p*X** than ***o*X** and ***m*X**, before reaching its saturation point, and the ***o*X** and ***m*X** uptake remained extremely low during the whole experiment (Figure 6a). The PXRD pattern of **EtP6***β* after exposure to this mixture of isomers matched the simulated

DOI: 10.1021/jacs.8b02621
J. Am. Chem. Soc. 2018, 140, 6921–6930

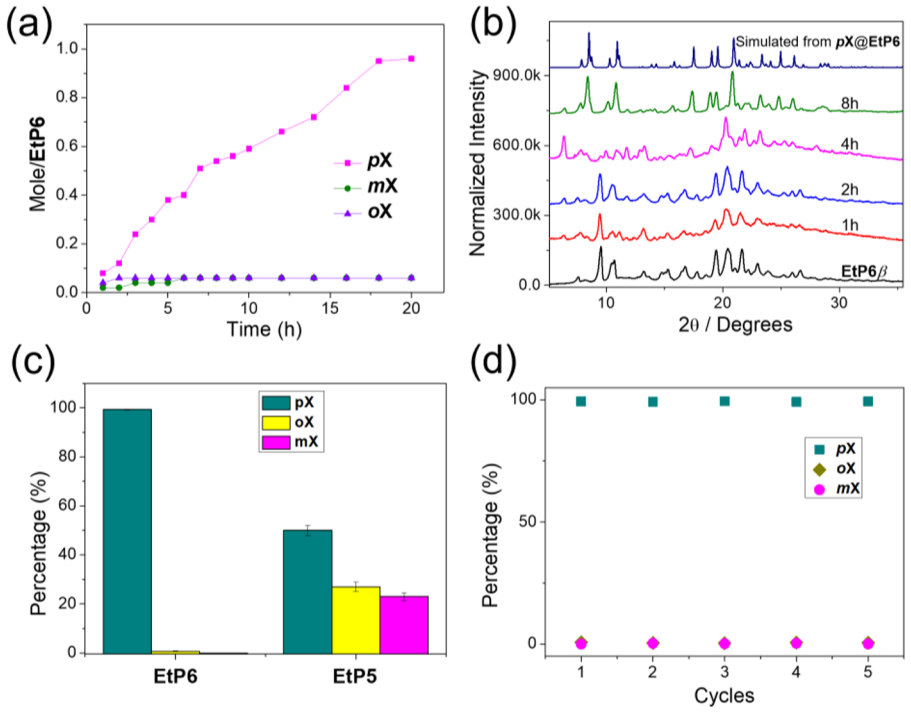

Figure 6. (a) Time-dependent **EtP6***β* solid−vapor sorption plot for 1:1:1 xylene isomers mixture vapor. (b) PXRD patterns of **EtP6***β* after being exposed to xylene isomers (1:1:1, v:v:v). (c) Relative xylene isomer uptake in **EtP6** and **EtP5** after 12 h upon surface removal using gas chromatography. (d) Percentage of ***p*X**, ***o*X** and ***m*X** in **EtP6** for 12 h after the same material is recycled 5 times.

PXRD pattern for ***p*X@EtP6** (Figure 6b). These results show that **EtP6***β* can selectively capture ***p*X** from a mixture of isomers as a crystalline solid via the transformation of **EtP6***β* into ***p*X@EtP6** (Figure 2f → 2b). We also used gas chromatography, which showed that the uptake of ***p*X** by **EtP6***β* was ∼90% after 12 h, whereas uptake of ***o*X** and ***m*X** accounts for the other 10% (Figure 6a and S28). We ascribe the low uptake of ***o*X** and ***m*X** to crystal surface adsorption. These solid-state adsorption experiments confirmed that **EtP6** can selectively capture ***p*X** in the solid state as well as from solution. The ***p*X** selectively of **EtP6** is comparable to the best-performing MOFs/zolites used for this application (Table S8).

We found that the purity of the ***p*X** could be further increased by adopting a surface removal procedure after adsorption of a mixed xylene vapor in **EtP6***β*. After adsorption of the vapor mixture, the **EtP6** solids were heated at 40 °C for 30 min to remove any unbound xylene isomer molecules physisorbed on the crystal surface (Figure S29). ***p*X** was then released from the selectively formed ***p*X@EtP6** phase with a purity of 99.1% (Figure 6c and S30). Interestingly, after the ***p*X** was completely removed from the ***p*X@EtP6** crystals, the desolvated ***p*X@EtP6** was shown by PXRD experiments to remain as **EtP6***β* (Figure 3a and S31).

A major problem in porous adsorbent technology is decreased performance over time, either because of fouling or instability of the porous framework. To be practically useful, ***p*X** should be separated with an extremely high purity and the adsorbent must perform well over many cycles without any degradation. We proved that the **EtP6***β* crystals could still capture ***p*X** selectively from a xylene mixture to form ***p*X@EtP6** in a second cycle (Figure 6d and S32); this process could be cycled at least 5 times without any loss of performance in the selective ***p*X** capture (Figure 6d). We believe that the adaptibility of these crystals allows them to "self-heal" over multiple use cycles, and pore collapse is not an issue because the materials are not permanently porous. Commercial grade xylene, produced by the methylation of toluene and benzene, usually contains about 40−65% of ***m*X** and up to 20% each of ***o*X**, ***p*X** and ethylbenzene (**EB**).[46] When commercial grade xylene (***o*X**:***m*X**:***p*X**:**EB** = 20:20:20:40, v:v) was tested, **EtP6***β* adsorbed 80.7% ***p*X** after one cycle. This selectivity was found lower than that in the 1:1:1 xylene mixture discussed above, which probably mostly arises from **EB** competing more effectively with ***p*X** than either ***m*X** or ***o*X** (Figure S35).

Conformation Search and Crystal Structure Prediction. Our X-ray diffraction studies suggested that conformational flexibility in **EtP6** might be the key to understanding its selective adsorption behavior. To explore this further, we carried out a computational search of the molecular conformational space, which showed a large number of energetically accessible conformers (Figure 7a). The lowest energy molecular geometries are characterized by arene and ethyl groups that are folded in to give compact conformers and therefore have a low radius of gyration (Figure 7a). This maximizes stabilizing nonbonded intramolecular contacts. By contrast, all of the observed crystal structures make use of more open conformers that provide fully expanded molecular cavities, as in ***o*X@EtP6**, or partially open cavities, as in ***p*X@EtP6** and ***m*X@EtP6**. The calculated gas phase conformers that are geometrically nearest to the conformations in the known phases of **EtP6** are indicated in Figure 7a.

To further investigate the energetic relationship between crystal forms, we used crystal structure prediction (CSP) and calculated the possible crystal structures available to each of the conformers found experimentally (Figure 7b, where each point corresponds to a local minimum in the lattice energy surface). All of the observed structures are located on the calculated energy landscapes, as indicated in Figure 7b. This shows that

DOI: 10.1021/jacs.8b02621
J. Am. Chem. Soc. 2018, 140, 6921−6930

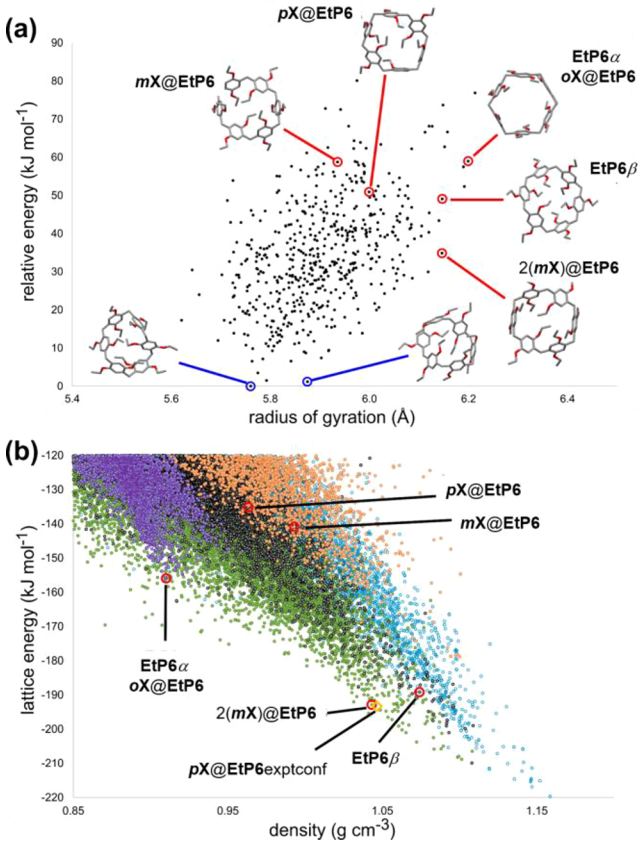

Figure 7. (a) Calculated conformational landscape for **EtP6**. Each point corresponds to a distinct conformer. Points encircled in red are those with lowest RMSD when compared to the conformations seen in observed crystal structures of **EtP6** and are labeled by the crystal form to which they correspond. Diagrams of the two lowest energy predicted, collapsed conformers (circled in blue) are shown. (b) Crystal structure prediction landscapes calculated from five of the observed conformers of **EtP6**: **EtP6***β* (black points); **EtP6***α* (purple points); ***m*X@EtP6** (orange points); 2(***m*X**)**@EtP6** (green points); ***p*X@EtP6** (light blue points). Each point corresponds to a distinct crystal structure (local lattice energy minimum) of pure **EtP6** (no guests were included in the calculations) and those corresponding to observed crystal structures are highlighted as red circles. The calculated structure of the artificially desolvated ***p*X@EtP6** with molecular geometry constrained at the in-crystal conformation (***p*X@EtP6**exptconf) is shown as an orange diamond.

the **EtP6** arrangement in each structure corresponds to a local energy minimum, even without including the xylene guest molecules in the calculations. The **EtP6***β* phase obtained by activation of the xylene solvates is relatively low in energy, but it is not the lowest energy guest-free structure of **EtP6** that is possible; several putative crystal structures are calculated to have lattice energies that are lower by up to 30 kJ mol^{-1}, even within this limited set of five molecular conformations. The **EtP6***α* structure, which has the same crystal packing of **EtP6** as the ***o*X@EtP6** structure, is one of the lowest energy crystal structures available for the conformation with a fully open molecular cavity and all-parallel arene rings (purple points in Figure 7a). The total lattice energy of this structure is high, but it is likely stabilized in ***o*X@EtP6** through host−guest interactions and entropic stabilization of the disordered ***o*X** guest. The conformer corresponding to the ***p*X@EtP6** crystal structure leads to the densest and most stable crystal structures in our computational study (blue points, Figure 7b). However, there is a significant distortion between this gas phase conformer and the experimental conformation found in ***p*X@EtP6**; two of the arene rings tilt further into the cavity in the gas phase conformation. Because of this difference in molecular geometries, a close geometric match to ***p*X@EtP6** is not found in the CSP set. The high-energy CSP-generated structure indicated in Figure 7b matches the structure obtained by substituting the experimental **EtP6** molecular geometry in ***p*X@EtP6** by the gas phase conformer without ***p*X**, followed by lattice energy minimization. To more accurately assess the lattice energy of ***p*X@EtP6**, we calculated the lattice energy with the molecular conformation constrained to the in-crystal geometry. The result of this calculation (orange diamond, Figure 7b) shows that the crystal packing of **EtP6** in ***p*X@EtP6** is almost equi-energetic to that found in 2(***m*X**)**@EtP6**. The strong dependence of the energy on the molecular geometry demonstrates that the flexibility of this conformer is important in determining the structure and stability of ***p*X@EtP6**. We cannot infer from this that there is no preferential thermodynamic driving force for the formation of ***p*X@EtP6** over 2(***m*X**)**@EtP6** because these CSP calculations exclude the guests. However, our kinetic studies for the three individual xylene isomers (Figure 5a) suggest that the preferential formation of ***p*X@EtP6** in the competitive adsorption process might be at least partly kinetic in origin.

Even though both pillararenes undergo rearrangements to closed, cavity-free structures during activation, we have shown experimentally and explained by computation that their conformers are adaptive. Hence, the host molecules can change conformation reversibly in the solid state to enable the selective adsorption of guest molecules. For example, CSP calculations reveal the energetic relationship between the unsolvated **EtP6** structures of the two ***m*X** solvates (Figure 7): the **EtP6** arrangement in the solution-grown 2(***m*X**)**@EtP6** is much lower in energy on the landscape of crystal structures. Indeed, the **EtP6** packing in ***m*X@EtP6** is calculated to be the highest energy of the experimentally observed structures, indicating that vapor sorption in crystalline **EtP6***β* leads to a relatively high-energy, kinetically stable structure. ***m*X@EtP6** has a molecular conformation that is very similar to **EtP6***β*, from which it is produced. This may therefore be the best structure that is accessible without a more significant structural rearrangement, which is not possible in the solid state.

CONCLUSIONS

We have investigated the shape selective properties of two easily obtained pillar[*n*]arenes, **EtP5** and **EtP6**, toward three xylene isomers. Adaptive **EtP6***β* crystals were found to efficiently capture ***p*X** from a xylene isomer mixture with high selectivity. We have used conformer searches and crystal structure prediction methods to understand the flexibility of this molecular crystal. Selectivity is an intrinsic property of the **EtP6** host, arising from the suitable size and shape of the **EtP6** cavity plus the flexibility of the **EtP6** conformer in the solid state. This adaptive behavior is comparable to certain MOFs, in which the pore structures can adapt in the presence of guest molecules. Though the separation of xylene isomers has been achieved in porous extended frameworks, such as zeolites[47,48] and MOFs,[10−15] this new molecular approach offers potential advantages. For example, **EtP6** is soluble, easy to synthesize, and has better chemical stability than many crystalline MOFs and COFs. Also, exposure to xylene transforms the structure of the adaptive material to the desired guest-loaded structure:

DOI: 10.1021/jacs.8b02621
J. Am. Chem. Soc. 2018, 140, 6921−6930

hence, loss of crystallinity caused from repeat adsorption cycles does not result in a loss in performance, and the separation is almost perfectly repeatable. Although the overall uptake capacity in **EtP6**β is lower than some porous extended frameworks, and the uptake kinetics are relatively slow, ***p*X** can be separated from ***o*X** and ***m*X** with high purity in just one cycle, which is desirable. Also, it is possible that the adsorption kinetics may become faster at the higher temperatures at which xylenes are typically produced.[8,46] Though **EtP5**α did not perform well for xylene separation, this molecule may have the potential to separate other hydrocarbons. Hydrocarbon separations using higher members of pillar[n]arenes (n = 7, 8, 9, 10) are also a target for future studies.

EXPERIMENTAL SECTION

Materials. Both **EtP5** and **EtP6** were synthesized as described previously.[28] Activated crystalline **EtP5**, **EtP5**α were recrystallized from tetrahydrofuran first and dried under vacuum at 60 °C overnight. Activated crystalline **EtP6**, **EtP6**β were obtained by heating up to 160 °C for 1 h. All xylene isomer mixtures are 1:1:1 (v/v/v).

Single Crystal Growth. When grown by solvent evaporation, 5 mg portions of dry **EtP5** or **EtP6** were transferred into small glass sample vials and dissolved in 2 mL of ***p*X**, ***m*X** or ***o*X**. The resultant homogeneous solutions were allowed to slowly evaporate at room temperature over 7 to 10 days to afford colorless crystals. Single crystals of **EtP6**β, suitable for SC-XRD, were isolated after heating a sample of ***p*X@EtP6** at 160 °C for 1 h. All other phase transormations were monitored by PXRD.

Xylene Vapor Adsorption Measurements. For each single-component or mixture of xylene isomers vapor-phase experiment, an open 5 mL vial containing 20 mg of guest-free **EtP5**α or **EtP6**β adsorbent was placed in a sealed 20 mL vial containing 1 mL of a single component or mixture of xylene isomers. Uptake by **EtP5**α or **EtP6**β crystals were measured each hour by completely dissolving the crystals, and measuring the ^{1}H NMR spectra to determine the ratio of each xylene isomer, with respect to **EtP5** or **EtP6**. In addtion, relative uptake in the **EtP5**α or **EtP6**β crystals were measured after 12 h using gas chromatography using a headspace method.

^{13}C Solid-State NMR. The ^{13}C solid-state NMR spectra were acquired at room temperature on a 9.4 T Bruker Avance III HDNMR spectrometer using a 4 mm HXY triple-resonance MAS probe (in double resonance mode) tuned to ^{1}H and ^{13}C at 400.1 and 100.6 MHz, respectively. The experiments were performed under magic angle spinning (MAS) at 12.5 kHz with a recycle delay of 3.5 s and using cross-polarization (CP) with a ^{13}C radio frequency (rf) field amplitude of 41 kHz ramped to obtain maximum signal at a ^{1}H rf field of approximately 65 kHz and with an optimized contact pulse of 1.5 ms. ^{1}H pulses and SPINAL-64 heteronuclear decoupling[49] during ^{13}C F_2 acquisition were performed at a rf field amplitude of 96 kHz whereas the ^{13}C pulses in the 2D z-filter refocused INADEQUATE[43,44] spectrum were performed at a rf field amplitude of 60 kHz. Additionally, the rotor synchronized echo and z-filter delays of the INADEQUATE experiment were experimentally optimized for best efficiency and found to be 3.2 and 0.8 ms, respectively. The 1D CP MAS spectrum was obtained with 2048 scans (experimental time 2 h) whereas the INADEQUATE spectrum[43] was acquired with 78 t_1 increments and the same number of scans (total experimental time 6.5 days). All data were processed with 5 Hz exponential line broadening, unless stated otherwise, and simulated with Topspin. The ^{13}C chemical shifts were externally referenced at room temperature to the CH_2 group of adamantane at 29.45 ppm.[50] Note that although ^{13}C CP MAS experiments are not quantitative, only ^{13}C integration within a chemically distinct carbon environment is only given as its similar nature allows carbon ratios to be appropriately estimated.

Conformer Search. Molecular conformers were generated using a low-mode conformational search (LMCS) method,[51,52] as implemented in MacroModel.[53] In the LMCS algorithm, a starting molecular geometry is initially optimized, subsequently perturbed along a random combination of its calculated normal modes and reoptimized. Newly generated molecular conformers are clustered on the fly. Because of the large number of energy evaluations and minimizations required for an exhaustive search, the initial conformer search was performed using a force field based methodology; we applied the OPLS3[54] force field, as implemented in Schrödinger.[55] To ensure conformational search was as complete as possible two sets with a total of 150 000 conformers were generated from two independent searches performed using minimum and maximum move distances of 6 and 12 Å. Conformational searches were started from the crystallographic molecular geometries of 2(***m*X**)**@EtP6**. Similar conformational space was sampled when the search was started from the unfolded **EtP6** conformer of **EtP6**α. Energy minimization was performed using the PRCG algorithm[56] and was considered converged when gradients were below 0.05 kJ/mol/Å. Duplicate molecular geometries were removed if all-atom RMS deviation of atomic positions, as implemented in MacroModel, was lower than 1.0 Å, which allows to reduce the vast number of conformers generated without losing completeness of the conformational space.

In our experience, significant inaccuracies in the description of the possible conformers can result from the use of a force field based methodology.[57] Therefore, a more accurate description was obtained by DFT-D reoptimization of all unique conformers within a 50 kJ/mol window of the OPLS3 global minimum. DFT-D geometry optimization was performed with the Gaussian 09 code[58] using the B3LYP[59,60] functional and 6-311G(d,p) basis set, using a tight DFT integration grid. Dispersion energy corrections were included using Grimme's D3 scheme with Becke and Johnson (BJ) damping.[61,62] The relative energy of a given conformer, at DFT-D level, was defined as the difference between its total gas phase DFT-D energy and the lowest total gas phase DFT-D energy of the molecular conformers. The radius of gyration of each DFT-D optimized conformer was calculated using BIOVIA's Materials Studio software.

Crystal Structure Prediction (CSP). Trial crystal structures were generated with one molecule in the asymmetric unit in the 30 most common space groups in which nonpolymeric organic molecular crystal structures are reported in the Cambridge Structure Database: $P2_1/c$; $P2_12_12_1$; $P\bar{1}$; $P2_1$; $Pbca$; $C2/c$; $Pna2_1$; Cc; $Pca2_1$; $C2$; $P1$; $Pbcn$; Pc; $P2_12_12$; $P4_32_12$; $P4_1$; $P3_2$; $Fdd2$; $Pccn$; $P2/c$; $P6_1$; $I4_1/a$; $R\bar{3}$; $C222_1$; $P4_2/n$; $P3_221$; $Aba2$; $P\text{-}32_1c$; $Iba2$ and $R3$. CSP was performed using a quasi-random sampling procedure, as implemented in the Global Lattice Energy Explorer software.[63] The generation of structures involves a low-discrepancy sampling of all structural variables within each space group: unit cell lengths and angles; molecular positions and orientations within the asymmetric unit. Space group symmetry was then applied and a geometric test was performed for overlap between molecules, which was removed by lattice expansion (the SAT-expand method in ref 56). All accepted trial structures were lattice energy minimized and the search was run until a total of 5000 lattice energy minimizations had been performed in each space group. Crystal structure prediction landscapes were calculated from five **EtP6** conformers observed in **EtP6**α, **EtP6**β, ***m*X@EtP6**, 2(***m*X**)**@EtP6** and ***p*X@EtP6** crystal structures. Initial crystallographic molecular geometries were optimized at the aforementioned DFT-D level. Molecular geometries were held rigid during crystal structure generation and lattice energy minimization. Trial structures were minimized following a two-step lattice energy minimization protocol. Structures were initially optimized applying an external pressure of 0.1 GPa, followed by a final lattice energy minimization after removal of the external pressure. Space group symmetry was constrained during both lattice energy minimization steps. Lattice energy minimizations were performed using an anisotropic atom−atom potential using DMACRYS.[64] Electrostatic interactions were modeled using CHLEPG point charges, as implemented in Gaussian09,[58] during the first lattice energy minimization and using an atomic multipole description[65] (up to hexadecapole) of the molecular charge distribution from the B3LYP/6-31G** calculated charge density using a distributed multipole analysis in the second lattice energy minimization. Atom−atom repulsion and dispersion interactions were modeled using the W99 model potential.[66] Charge−charge, charge−dipole and dipole−

DOI: 10.1021/jacs.8b02621
J. Am. Chem. Soc. 2018, 140, 6921−6930

dipole interactions were calculated using Ewald summation, whereas all other intermolecular interactions were summed to a 30 Å cutoff between molecular centers-of-mass. For a given molecule, relative (lattice) energy of a given predicted crystal structure was evaluated as the difference between its calculated lattice energy and lattice energy of the global minima on the energy vs density landscape of that given molecule. Duplicate structures were removed from the set using COMPACK,[67] based on matching interatomic distances within 30 molecule clusters.

The lattice energy of ***p*X@EtP6** with the molecular geometry constrained at the experimental in-crystal conformation was evaluated by first performing a constrained single molecule geometry optimization with all torsion angles determining the orientation of the arene rings fixed from the X-ray crystal structure. The resulting molecular geometry was substituted into the experimental ***p*X@EtP6** crystal structure (after removal of ***p*X**) and a rigid molecule lattice energy minimization was performed. The molecular geometry optimization and lattice energy minimization used identical computational methods (functional, basis set, force field and cutoffs) to those used in the conformer search and CSP.

■ ASSOCIATED CONTENT

Supporting Information

The Supporting Information is available free of charge on the ACS Publications website at DOI: 10.1021/jacs.8b02621.

Experimental details, crystallography, and other materials (PDF)
X-ray crystallographic data for **EtP5** (CIF)
X-ray crystallographic data for 2(**EtP5**)·3.49(***m*X**) (CIF)
X-ray crystallographic data for **EtP5**·***p*X** (CIF)
X-ray crystallographic data for **EtP6**·***o*X** (CIF)
X-ray crystallographic data for **EtP6**·2(***m*X**) (CIF)
X-ray crystallographic data for **EtP6**·***p*X** (CIF)
X-ray crystallographic data for **EtP6** (CIF)
X-ray crystallographic data for **EtP6**·***m*X** (CIF)

■ AUTHOR INFORMATION

Corresponding Authors

*fhuang@zju.edu.cn
*G.M.Day@soton.ac.uk
*aicooper@liverpool.ac.uk

ORCID

Tomoki Ogoshi: 0000-0002-4464-0347
Frédéric Blanc: 0000-0001-9171-1454
Graeme M. Day: 0000-0001-8396-2771
Feihe Huang: 0000-0003-3177-6744
Andrew I. Cooper: 0000-0003-0201-1021

Author Contributions

⊥K.J. and M.L. contributed equally.

Notes

The authors declare no competing financial interest.

■ ACKNOWLEDGMENTS

This work was supported by the National Natural Science Foundation of China (21434005, 91527301). The authors gratefully acknowledge the Engineering and Physical Sciences Research Council (EP/N004884/1, EP/H000925/1, and Doctoral Training Studentships to A.R.H.), and the European Research Council under the European Union's Seventh Framework Programme (FP/2007-2013)/ERC through grant agreement numbers 321156 (ERC-AG-PE5-ROBOT) and 307358 (ERC-stG-2012-ANGLE), for funding. We thank Diamond Light Source for access to beamlines I19 (MT15777) and Harriott Nowell for her assistance during this experiment, and I11 (EE12336 and EE17193). We acknowledge the use of the IRIDIS High Performance Computing Facility, and associated support services at the University of Southampton, in the completion of this work. We also acknowledge the ARCHER UK National Supercomputing Service which was accessed via the UK's HPC Materials Chemistry Consortium membership, which is funded by the EPSRC (EP/L000202).

■ REFERENCES

(1) Scheirs, J.; Long, T. E. *Industrial Modern Polyesters: chemistry and technology of polyesters and copolyesters*; Wiley: Chichester, 2003.
(2) Sholl, D. S.; Lively, R. P. *Nature* **2016**, *532*, 435.
(3) Flick, E. W. *Industrial Solvent Handbook*, 5th ed.; Noyes Data Corporation: Westwood, NJ, 1998.
(4) Rao, K. V.; Jayaramulu, K.; Maji, T. K.; George, S. J. *Angew. Chem., Int. Ed.* **2010**, *49*, 4218.
(5) Minceva, M.; Rodrigues, A. E. *AIChE J.* **2007**, *53*, 138.
(6) Mohameed, H. A.; Jdayil, B. A.; Takrouri, K. *Chem. Eng. Process.* **2007**, *46*, 25.
(7) Cottier, V.; Bellat, J.-P.; Simonot-Grange, M.-H.; Methivier, A. *J. Phys. Chem. B* **1997**, *101*, 4798.
(8) Meyers, R. *Handbook of Petroleum Refining Processes*, 3th ed.; McGraw-Hill: New York, NY, 2003; pp 2.47−2.53.
(9) Ruthven, D. *Principles of Adsorption and Adsorption Processes*; Wiley: New York, NY, 1984; pp 401−405.
(10) Warren, J. E.; Perkins, C. G.; Jelfs, K. E.; Boldrin, P.; Chater, P. A.; Miller, G. J.; Manning, T. D.; Briggs, M. E.; Stylianou, K. C.; Claridge, J. B.; Rosseinsky, M. J. *Angew. Chem., Int. Ed.* **2014**, *53*, 4592.
(11) Lusi, M.; Barbour, L. J. *Angew. Chem., Int. Ed.* **2012**, *51*, 3928.
(12) Holcroft, J. M.; Hartlieb, K. J.; Moghadam, P. Z.; Bell, J. G.; Barin, G.; Ferris, D. P.; Bloch, E. D.; Algaradah, M. M.; Nassar, M. S.; Botros, Y. Y.; Thomas, K. M.; Long, J. R.; Snurr, R. Q.; Stoddart, J. F. *J. Am. Chem. Soc.* **2015**, *137*, 5706.
(13) Gu, Z.-Y.; Yan, X.-P. *Angew. Chem., Int. Ed.* **2010**, *49*, 1477.
(14) Barcia, P. S.; Guimaraes, D.; Mendes, P. A. P.; Silva, J. A. C.; Guillerm, V.; Chevreau, H.; Serre, C.; Rodrigues, A. E. *Microporous Mesoporous Mater.* **2011**, *139*, 67.
(15) Alaerts, L.; Maes, M.; Giebeler, L.; Jacobs, P. A.; Martens, J. A.; Denayer, J. F. M.; Kirschhock, E. A.; De Vos, D. E. *J. Am. Chem. Soc.* **2008**, *130*, 14170.
(16) Mitra, T.; Jelfs, K. E.; Schmidtmann, M.; Ahmed, A.; Chong, S. Y.; Adams, D. J.; Cooper, A. I. *Nat. Chem.* **2013**, *5*, 276.
(17) Ogoshi, T.; Kanai, S.; Fujinami, S.; Yamagishi, T. A.; Nakamoto, Y. *J. Am. Chem. Soc.* **2008**, *130*, 5022.
(18) Xue, M.; Yang, Y.; Chi, X.; Zhang, Z.; Huang, F. *Acc. Chem. Res.* **2012**, *45*, 1294.
(19) Ogoshi, T.; Yamagishi, T.-a.; Nakamoto, Y. *Chem. Rev.* **2016**, *116*, 7937.
(20) Cao, D.; Kou, Y.; Liang, J.; Chen, Z.; Wang, L.; Meier, H. *Angew. Chem., Int. Ed.* **2009**, *48*, 9721.
(21) Li, H.; Chen, D.-X.; Sun, Y.-L.; Zheng, Y.; Tan, L.-L.; Weiss, P. S.; Yang, Y.-W. *J. Am. Chem. Soc.* **2013**, *135*, 1570.
(22) Ji, X.-F.; Xia, D.-Y.; Yan, X.; Wang, H.; Huang, F.-H. *Acta Polym. Sin.* **2017**, 9.
(23) Zhao, Q.; Dunlop, J. W. C.; Qiu, X.; Huang, F.; Zhang, Z.; Heyda, J.; Dzubiella, J.; Antonietti, M.; Yuan, J. *Nat. Commun.* **2014**, *5*, 4293.
(24) Li, S.-H.; Zhang, H.-Y.; Xu, X.; Liu, Y. *Nat. Commun.* **2015**, *6*, 7590.
(25) Strutt, N. L.; Zhang, H.; Schneebeli, S. T.; Stoddart, J. F. *Acc. Chem. Res.* **2014**, *47*, 2631.
(26) Ogoshi, T.; Kida, K.; Yamagishi, T.-a. *J. Am. Chem. Soc.* **2012**, *134*, 20146.
(27) Jie, K.; Zhou, Y.; Yao, Y.; Shi, B.; Huang, F. *J. Am. Chem. Soc.* **2015**, *137*, 10472.

DOI: 10.1021/jacs.8b02621
J. Am. Chem. Soc. 2018, 140, 6921−6930

(28) Hu, X.-B.; Chen, Z.; Chen, L.; Zhang, L.; Hou, J.-L.; Li, Z.-T. *Chem. Commun.* **2012**, *48*, 10999.
(29) Talapaneni, S. N.; Kim, D.; Barin, G.; Buyukcakir, O.; Je, S. H.; Coskun, A. *Chem. Mater.* **2016**, *28*, 4460.
(30) Duan, Q.; Cao, Y.; Li, Y.; Hu, X.; Xiao, T.; Lin, C.; Pan, Y.; Wang, L. *J. Am. Chem. Soc.* **2013**, *135*, 10542.
(31) Jie, K.; Zhou, Y.; Li, E.; Li, Z.; Zhao, R.; Huang, F. *J. Am. Chem. Soc.* **2017**, *139*, 15320.
(32) Zhang, Z.; Xia, B.; Han, C.; Yu, Y.; Huang, F. *Org. Lett.* **2010**, *12*, 3285.
(33) Zhang, Z.; Luo, Y.; Chen, J.; Dong, S.; Yu, Y.; Ma, Z.; Huang, F. *Angew. Chem., Int. Ed.* **2011**, *50*, 1397.
(34) Gao, B.; Tan, L.-L.; Song, N.; Li, K.; Yang, Y.-W. *Chem. Commun.* **2016**, *52*, 5804.
(35) Tan, L.-L.; Li, H.; Tao, Y.; Zhang, S. X.-A.; Wang, B.; Yang, Y.-W. *Adv. Mater.* **2014**, *26*, 7027.
(36) Ogoshi, T.; Sueto, R.; Yoshikoshi, K.; Yamagishi, T.-a. *Chem. Commun.* **2014**, *50*, 15209.
(37) Tan, L.-L.; Zhu, Y.; Long, H.; Jin, Y.; Zhang, W.; Yang, Y.-W. *Chem. Commun.* **2017**, *53*, 6409.
(38) Singh, Z. V.; Tan, L.-L.; Cowan, M. G.; Yang, Y.-W.; Zhang, W.; Gin, D. L.; Noble, R. D. *J. Membr. Sci.* **2017**, *539*, 224.
(39) Jie, K.; Liu, M.; Zhou, Y.; Little, M.; Bonakala, S.; Chong, S.; Stephenson, A.; Chen, L.; Huang, F.; Cooper, A. I. *J. Am. Chem. Soc.* **2017**, *139*, 2908.
(40) Jie, K.; Zhou, Y.; Li, E.; Zhao, R.; Liu, M.; Huang, F. *J. Am. Chem. Soc.* **2018**, *140*, 3190.
(41) Bennett, T. D.; Cheetham, A. K.; Fuchs, A. H.; Coudert, F.-X. *Nat. Chem.* **2017**, *9*, 11.
(42) Silverstein, R. M.; Webster, F. X.; Kiemle, D. J. *The Spectrometric Identification of Organic Compounds*; John Wiley & Sons: New York, NY, 2005.
(43) Lesage, A.; Bardet, M.; Emsley, L. *J. Am. Chem. Soc.* **1999**, *121*, 10987.
(44) Harris, R. K.; Cadars, S.; Emsley, L.; Yates, J. R.; Pickard, C. J.; Jetti, R. K. R.; Griesser, U. J. *Phys. Chem. Chem. Phys.* **2007**, *9*, 360.
(45) Perry, A. *Oper. Res.* **1978**, *26*, 1073.
(46) Fabri, J.; Graeser, U.; Simo, T. A. *Ullmann's Encyclopedia of Industrial Chemistry*; Wiley-VCH: Weinheim, Germany, 2000.
(47) Lai, Z.; Bonilla, G.; Diaz, I.; Nery, J. G.; Sujaoti, K.; Amat, M. A.; Kokkoli, E.; Terasaki, O.; Thompson, R. W.; Tsapatsis, M.; Vlachos, D. G. *Science* **2003**, *300*, 456.
(48) Kim, D.; Jeon, M. Y.; Stottrup, B. L.; Tsapatsis, M. *Angew. Chem., Int. Ed.* **2018**, *57*, 480.
(49) Fung, B. M.; Khitrin, A. K.; Ermolaev, K. *J. Magn. Reson.* **2000**, *142*, 97.
(50) Morcombe, C. R.; Zilm, K. W. *J. Magn. Reson.* **2003**, *162*, 479.
(51) Kolossváry, I.; Guida, W. C. *J. Am. Chem. Soc.* **1996**, *118*, 5011.
(52) Kolossváry, I.; Guida, W. C. *J. Comput. Chem.* **1999**, *20*, 1671.
(53) Mohamadi, F.; Richards, N. G. J.; Guida, W. C.; Liskamp, R.; Lipton, M.; Caufield, C.; Chang, G.; Hendrickson, T.; Still, W. C. *J. Comput. Chem.* **1990**, *11*, 440.
(54) Harder, E.; Damm, W.; Maple, J.; Wu, C.; Reboul, M.; Xiang, J. Y.; Wang, L.; Lupyan, D.; Dahlgren, M. K.; Knight, J. L.; Kaus, J. W.; Cerutti, D. S.; Krilov, G.; Jorgensen, W. L.; Abel, R.; Friesner, R. A. *J. Chem. Theory Comput.* **2016**, *12*, 281.
(55) *MacroModel*, V10.4.017, Release 2015-4; Schrodinger LLC: New York, NY, 2015.
(56) Perry, A. *Oper. Res.* **1978**, *26*, 1073.
(57) Thompson, H. P. G.; Day, G. M. *Chem. Sci.* **2014**, *5*, 3173.
(58) Frisch, M. J.; Trucks, G. W.; Schlegel, H. B.; Scuseria, G. E.; Robb, M. A.; Cheeseman, J. R.; Scalmani, G.; Barone, V.; Mennucci, B.; Petersson, G. A.; Nakatsuji, H.; Caricato, M.; Li, X.; Hratchian, H. P.; Izmaylov, A. F.; Bloino, J.; Zheng, G.; Sonnenberg, J. L.; Hada, M.; Ehara, M.; Toyota, K.; Fukuda, R.; Hasegawa, J.; Ishida, M.; Nakajima, T.; Honda, Y.; Kitao, O.; Nakai, H.; Vreven, T.; Montgomery, J. A.; Peralta, J. J. E.; Ogliaro, F.; Bearpark, M.; Heyd, J. J.; Brothers, E.; Kudin, K. N.; Staroverov, V. N.; Kobayashi, R.; Normand, J.; Raghavachari, K.; Rendell, A.; Burant, J. C.; Iyengar, S. S.; Tomasi, J.; Cossi, M.; Rega, N.; Millam, J. M.; Klene, M.; Knox, J. E.; Cross, J. B.; Bakken, V.; Adamo, C.; Jaramillo, J.; Gomperts, R.; Stratmann, R. E.; Yazyev, O.; Austin, A. J.; Cammi, R.; Pomelli, C.; Ochterski, J. W.; Martin, R. L.; Morokuma, K.; Zakrzewski, V. G.; Voth, G. A.; Salvador, P.; Dannenberg, J. J.; Dapprich, S.; Daniels, A. D.; Farkas, O.; Foresman, J. B.; Ortiz, J. V.; Cioslowski, J.; Fox, D. J. *Gaussian 09*, Revision D.01; Gaussian Inc.: Wallingford, CT, 2009.
(59) Becke, A. D. *J. Chem. Phys.* **1993**, *98*, 5648.
(60) Lee, C.; Yang, W.; Parr, R. G. *Phys. Rev. B: Condens. Matter Mater. Phys.* **1988**, *37*, 785.
(61) Grimme, S.; Antony, J.; Ehrlich, S.; Krieg, H. *J. Chem. Phys.* **2010**, *132*, 154104.
(62) Grimme, S.; Ehrlich, S.; Goerigk, L. *J. Comput. Chem.* **2011**, *32*, 1456.
(63) Case, D. H.; Campbell, J. E.; Bygrave, P. J.; Day, G. M. *J. Chem. Theory Comput.* **2016**, *12*, 910.
(64) Price, S. L.; Leslie, M.; Welch, G. W. A.; Habgood, M.; Price, L. S.; Karamertzanis, P. G.; Day, G. M. *Phys. Chem. Chem. Phys.* **2010**, *12*, 8478.
(65) Stone, A. J. *Chem. Phys. Lett.* **1981**, *83*, 233.
(66) Williams, D. E. *J. Comput. Chem.* **2001**, *22*, 1.
(67) Chisholm, J. A.; Motherwell, S. *J. Appl. Crystallogr.* **2005**, *38*, 228.

DOI: 10.1021/jacs.8b02621
J. Am. Chem. Soc. 2018, 140, 6921−6930